

Harmonizing Graphene Laminate Spacing and Zinc-Ion Solvated Structure toward Efficient Compact Capacitive Charge Storage

Jinrong Luo, Liang Xu, Haiming Liu, Yusong Wang, Qing Wang, Yanyan Shao, Menglei Wang, Dongzi Yang, Shuo Li, Liang Zhang, Zhou Xia, Tao Cheng,* and Yuanlong Shao*

Aqueous Zn-ion hybrid capacitors (ZIHCs) present prominent potentials in flexible wearable electronics application scenarios due to their inherent high safety and low cost. Simultaneously, volumetric energy density is one of the crucial parameters to determine the lifespan of the wearable electronics, in which light-weight and miniaturization is a cardinal prerequisite for realistic application. In this work, an aqueous ZIHC is constructed by harmonizing interlayer spacing of the laminate graphene film and Zn-ion solvation structure to improve the electrode space utilization. Laminate graphene film interspacing has been customized in the range of 0.72–0.81 nm via regulating the ratio of crumple graphene mediator, thereby optimizing the transport kinetics of large size hydrated Zn ions. Zn-ion solvation structure is further tailored by introducing ZnCl_2 electrolyte salt to accouple such regulated laminar ionic transport channel. In a result, the thus-derived ZIHC demonstrates an ultralong cycling lifespan of 100 000 cycles (93.9% capacitance retention), a preeminent volumetric capacitance (235.4 F cm^{-3}), and a remarkable specific area capacitance contribution ($C_{\text{ssa}} \approx 72 \text{ } \mu\text{F cm}^{-2}$). Quasi-solid-state ZIHC is assembled with ZnCl_2 solution-filled polyacrylamide gel electrolyte to concurrently achieve a superior areal capacitance of 1227 mF cm^{-2} and great mechanical flexibility toward practical wearable application.

1. Introduction

In combination with the complementary electrochemical feature of classic batteries and supercapacitors, hybrid capacitors have attracted extensive attention with the potential to deliver considerable energy density while maintaining a good rate capability and cycling life.^[1–5] Among various metal-ion systems, aqueous Zn-ion hybrid capacitors (ZIHC) are expected to be a promising solution as power supply component of the emerging flexible or wearable electronics, depending on the intrinsic merits of superior safety and low-cost.^[6–10] A representative aqueous ZIHC constitutes a Zn metal anode and a capacitive carbon-based cathode.^[11] With the merits of remarkable volumetric ($5855 \text{ vs } 2061 \text{ mAh cm}^{-3}$ for Li), gravimetric (823 mAh g^{-1}) capacity, and fast Zn stripping/plating dynamics, the metallic Zn has been verified as an outstanding anode to guarantee the fascinating energy density of aqueous ZIHC.^[12–15] Simul-

taneously, with the reversible electrostatic Zn ion adsorption/desorption charge storage mechanism, carbon-based cathode endows with superb power density and excellent cycling stability over 100 000 cycles. In this regard, by virtue of extremely high surface area and great conductivity, a series of highly porous carbon materials, such as activated carbon,^[16] carbon-derived carbon,^[17] carbon nanocages,^[18,19] and graphene^[20–22] have been demonstrated as cathode materials with promising gravimetric energy density. However, in regard to flexible and wearable electronics application scenarios, volumetric energy density is more crucially important to maximize the energy storage capability in limited configuration space.

To date, plentiful endeavor has been put forward in volumetric energy density optimization.^[23,24] Optimizing pore size of compact electrode material to couple with electrolyte ion size has been demonstrated as an efficient strategy to promote volumetric capacitance via maximizing electrode space utilization for electric double layer capacitors.^[25,26] For instance, the highest achievable normalized electrostatic capacitance could be achieved while porous carbon pore size well matches with bare ion size in ionic liquid-based supercapacitors.^[25,27] As for

J. R. Luo, Y. Y. Shao, M. L. Wang, D. Z. Yang, S. Li, L. Zhang, Z. Xia, Y. L. Shao
College of Energy Soochow Institute for Energy and Materials
Innovations (SIEMIS)

Key Laboratory of Advanced Carbon Materials and Wearable Energy
Technologies of Jiangsu Province

Soochow University

Suzhou 215006, P. R. China

E-mail: yishao@suda.edu.cn

L. Xu, T. Cheng

Institute of Functional Nano and Soft Materials (FUNSOM)

Soochow University

Suzhou 215123, P. R. China

E-mail: tcheng@suda.edu.cn

H. M. Liu, Q. Wang

School of Physical Science and Technology

ShanghaiTech University


Shanghai 201210, P. R. China

Y. S. Wang

Hefei National Laboratory for Physical Sciences at the Microscale

University of Science and Technology of China

Hefei 230026, P. R. China

 The ORCID identification number(s) for the author(s) of this article
can be found under <https://doi.org/10.1002/adfm.202112151>.

DOI: 10.1002/adfm.202112151

aqueous ZIHC, the capacitive porous carbon cathode accumulate electric charge mainly depends on the electrostatic counter ion adsorption.^[28] In addition, Zn^{2+} tends to form into hexahydrate structure ($[\text{Zn}(\text{H}_2\text{O})_6]^{2+}$) with ion size expansion from 1.48 to 8.6 Å via intense Coulombic interacting with surrounding water molecules.^[29,30] Due to the ion sieving effects, the inaccessibility of solvated $[\text{Zn}(\text{H}_2\text{O})_6]^{2+}$ in micropores will result in a severe loss of space utilization.^[31] Furthermore, the accessibility of the solvated Zn^{2+} into microporous carbon electrode will also have significant influence on the interfacial ion transport dynamics, ion transference number, and even the electrochemical process on the surface of counter Zn metal anode. Hence, harmonizing the pore geometry of carbon material to adapt solvated Zn^{2+} is meaningful toward densely packed Zn-ion storage. Nonetheless, it's still a great challenge to construct dense electrode materials with ordered porous structure in subnano scale while maintaining favorable ion transportation and efficient Zn^{2+} storage.

Among the numerous nanocarbon materials, graphene is likely to form into compact conductive carbon electrode with tunable laminate interlayer spacing,^[32] which is favorable for accommodating the solvated Zn^{2+} size to maximize the volumetric capacity. Herein, we deliberately harmonize the interlayer spacing of graphene laminate electrode and solvated Zn^{2+} via precise adjustment of electrode interlayer spacing and scrutinizing solvation size of Zn salt electrolytes. The thus-derived ZIHC displays an ultralong cycling lifespan of 100 000 cycles with an extremely high retention of $\approx 94\%$ and superb volumetric capacitance of 235.4 F cm^{-3} . The fabulous volumetric performance is mainly attributed to good Zn-ion transport kinetics in the regulated laminate space, and the subsequently unprecedented specific area capacitance (C_{ssa}) of $72 \mu\text{F cm}^{-2}$. As a result, the quasi-solid-state ZIHC was assembled in such regulated laminate graphene electrode and Zn-ion system, which delivered an exceptional areal capacitance of 1227 mF cm^{-2} .

2. Results and Discussion

Considering the cathode of ZIHCs mainly relies on Zn ion adsorption at the carbon material/electrolyte interface for charge storage, the microstructure of carbon electrode dominates the adsorption/desorption and even transport dynamics of Zn ion during the electrochemical process. Consequently, a compact carbon material with ordered pore size adapting 0.86 nm of solvated Zn-ion ($[\text{Zn}(\text{H}_2\text{O})_6]^{2+}$) could enhance volumetric capacitance with packing the solvated Zn-ions densely and neatly. As illustrated in **Figure 1a**, the interlayer spacing of laminate graphene film is first extended slightly by tailoring the mixing ratio of crumple NHG (obtained from hydrazine hydrate/ammonia thermal reduction of GO solution, named as N_2H_4 -Graphene, NHG) and GO flakes dispersion with subsequently vacuum-assisted assembly. As demonstrated in a series of basic physicochemical characterization (Figures S1 and S2, Supporting Information), NHG flakes exhibited typically reduction feature and crumple geometric configuration. The atomic force microscopic (AFM) results depicted that the crumple NHG flake presents $\approx 3 \text{ nm}$ fluctuation, which is significantly different with the flat GO sheets. Such 3 nm

fluctuation promises the NHG flake as spring-like spacer to tune the average interspacing of NHG-GO hybrid film. X-ray diffraction (XRD) patterns reflected the average interlayer spacing difference of the thus-fabricated various laminate graphene films (**Figure 1b**). Pure GO film exhibited an intense peak located at 12.3° , corresponding to the interlayer spacing of 0.72 nm. Subsequently, as the increasing of NHG sheets ratio, this corresponding (002) diffraction peak shift to a lower angle of 10.9° , which indicates the interspacing extension increased to 0.81 nm. The gradually broadening of the dominant peak is attributed to the wrinkle NHG sheets restacking. When the ratio of NHG sheet reaches to 90%, there is no distinct (002) diffraction peak detected at the low angle region in XRD pattern (**Figure S4**, Supporting Information), which indicates that the severe disturbance of the high ratio crumple NHG flakes hinder the formation of neat interlayer spacing.

Simultaneously, the hydrogen iodide (HI) reduction has been proved to be an efficient approach to synchronously fix the compact interval interlayer spacing and sufficient reduction of hybrid GO film.^[33] Thus, the as-synthesized NHG-GO hybrid films were then subjected to HI solution to immobilize the tailored interval spacing with the effects of nucleophilic substitution. **Figure 1c** displays a series of cross-sectional SEM images of reduced GO (rGO), NHG-rGO hybrid, and NHG films, which have uniform laminar feature. The rGO film demonstrates flat and densely packed morphology, while NHG-rGO hybrid and NHG films presents relatively corrugated sheets and extended interlayer gaps because of the increasing ratio of NHG wrinkled flakes. Even after HI reduction, NHG sheets continue acting as a trestle, preventing rGO sheets from aggregation and prolonging the average interlayer spacing. N_2 adsorption-desorption measurements suggest that the specific surface area (SSA) of NHG-rGO films ranges from 12.5 to $325.1 \text{ m}^2 \text{ g}^{-1}$ by varying the NHG content as summarized in **Table S1**, Supporting Information, whereas the corresponding packing density decreased from 1.58 to 1.0 g cm^{-3} (**Figure 1d**). Additionally, 75% NHG/rGO hybrid film presents a precipitous rise in adsorption isotherms within the relative pressure region (P/P_0) lower than 0.01, which further demonstrates more plentiful slit micropores created with NHG flake ratio rising to 75% (**Figure S5**, Supporting Information).

Solid-state nuclear magnetic resonance (NMR) spectroscopy has been demonstrated as one remarkable experimental technique to provide atomic-scale information about the local environments of adsorbed species.^[34,35] Because of aromatic ring current induced local magnetic field, the species near the carbon surface are shielded and shifted to lower frequency by several ppm as compared to free species.^[36] The ring current and subsequently induced chemical shift is nucleus independent. Thus, the nucleus independent chemical shift can serve as a typical indicator to illustrate electrolyte species state, such as distinguishing electrolyte species strongly adsorbed on the carbon surfaces inside the micropores (referred to as “in-pore”) from those species weakly adsorbed on or outside carbon particles (referred to as “ex-pore”).^[37] Here, we took solid-state ^1H magic angle spinning (MAS)-NMR spectroscopy to study the adsorption state of aqueous electrolyte inside thus-prepared rGO and NHG-rGO hybrid films with variable interlayer spacing.

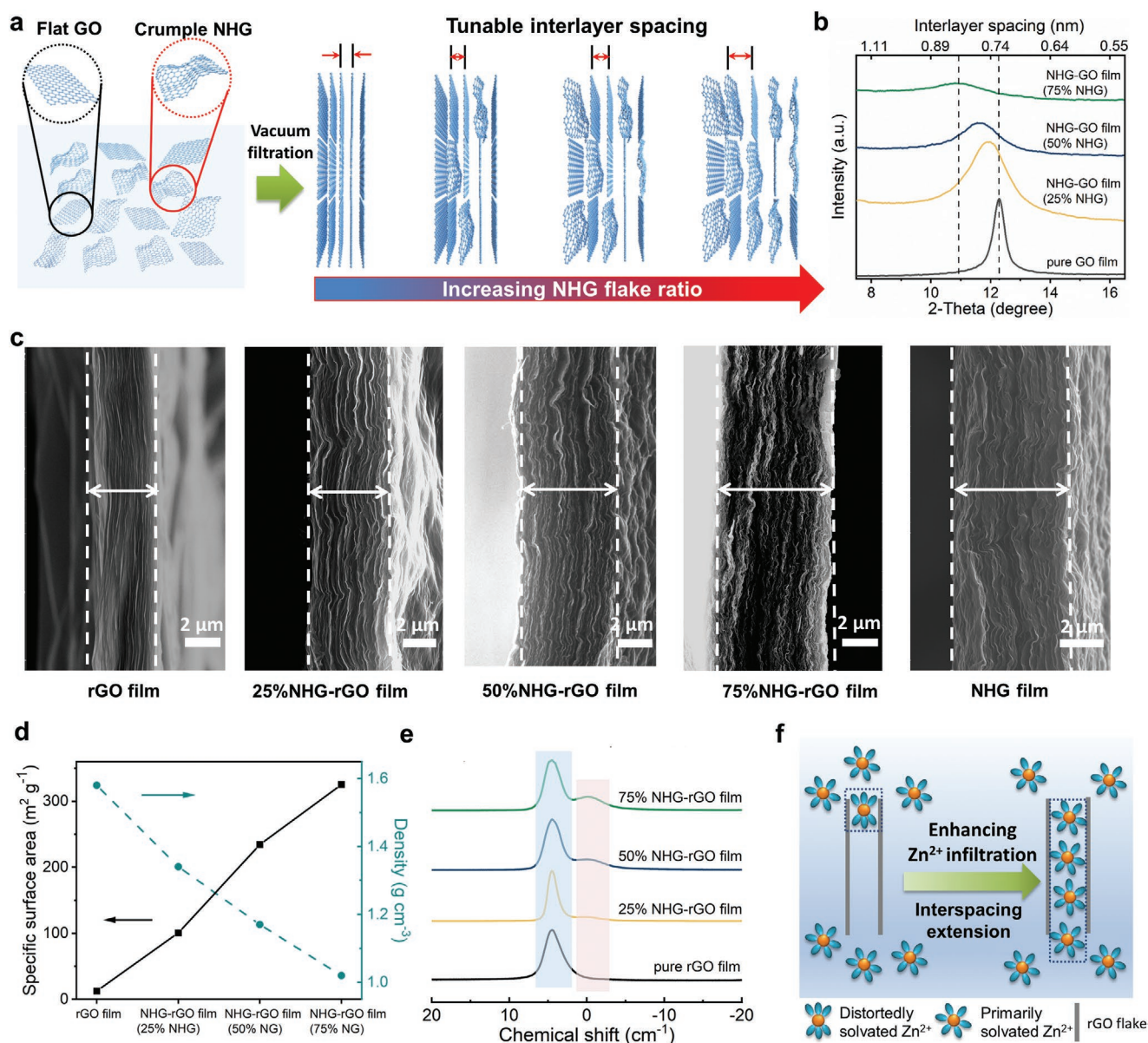


Figure 1. a) Schematic illustration of the preparation of NHG-GO films from GO and NHG solutions with a tunable ratio of NHG to GO. b) X-ray diffraction patterns of prepared films. c) Cross-sectional SEM images of rGO, rGO-NHG hybrid, and NHG films. d) Trade-off relationship between specific surface area and density. e) ^1H MAS solid-state-NMR spectra of different films soaked with ZnSO_4 electrolyte. f) Schematic diagram illustrating the influence of interspacing on space utilization.

Figure 1e displays the ^1H MAS-NMR spectra of various graphene film mixed with 2 M ZnSO_4 aqueous electrolyte with mass ratio of 1:1.5. Two typical broad resonance peaks located at chemical shifts of 4.45 and -0.11 ppm indicates weakly absorbed “ex-pore” electrolyte species and firmly adsorbed “in-pore” counterparts, respectively. As illustrated in Figure 1f, with the narrow interlayer spacing of 0.71 nm, the compact rGO film could be only accessed by a handful of distortedly solvated Zn-ion ($[\text{Zn}(\text{H}_2\text{O})_6]^{2+}$) as proved by the absence of the “in-pore” peak. With the gradually expansion of the average interlayer spacing to 0.81 nm (approaching to 0.86 nm of the fully solvated Zn-ion), the NHG-rGO hybrid films conspicuously demonstrate enhanced “in-pore” peak intensity (Table S2,

Supporting Information), which represents the significantly improved accessibility of aqueous electrolyte into graphene electrodes. The enhanced electrolyte infiltration and electrolyte ions confinement could be greatly feasible for promoting electrode space utilization and electrolyte dynamics.

To further demonstrate the varied interlayer spacing effect on Zn-ion storage, we systematically characterized the electrochemical performance of ZIHs with various NHG-rGO hybrid and rGO electrodes in 2 M ZnSO_4 electrolyte via a series of cyclic voltammogram (CV), galvanostatic charging/discharging (GCD), and electrochemical impedance spectroscopy (EIS) in the voltage window of 0.3–1.6 V (Figures S7–S9, Supporting Information). Figure S10a, Supporting Information, exhibits

the CV curve comparison of various NHG-rGO hybrid films with rGO electrode, where 75% NHG-rGO hybrid electrode shows the largest curve area among all the laminate electrodes with typical rectangular-like curve shape, indicating outstanding charge storage capability and ideal capacitive behavior. In contrast, with the decrease of interlayer spacing, the CV curves of the graphene electrodes gradually deviate from the ideal rectangle shape and shrunken curve areas, which represents inferior capacitive Zn-ion storage capability. **Figure 2a** summarized the gravimetric capacitance (C_{wt}) and rate capability, in which 75% NHG-rGO film electrode presents the highest C_{wt} of 198 F g^{-1} at 0.1 A g^{-1} and optimized capacitance retention of 74.4%; even current density increased to 20 A g^{-1} among all electrodes. As demonstrated in Figure S10b, Supporting Information, 75% NHG-rGO electrode still presented the highest C_{vol} of 198 F cm^{-3} at 0.1 A g^{-1} , even after taking electrode density into consideration. Although 50% NHG-rGO electrode also exhibited great C_{vol} of 190.9 F cm^{-3} at 0.1 A g^{-1} , it only displays a capacity retention of 66.8%, which is inferior to 74.4% for 75%

NHG-rGO electrode. Thus, according to the extended interlayer spacing, additional access of solvated Zn-ion and broadened electrolyte transport channels of the 75% NHG-rGO hybrid electrode significantly promote the Zn-ion storage capability and ion transport dynamics.

To further investigate the effect of interlayer spacing on capacity and rate capability, we performed EIS and capacitance differentiation analysis to characterize the ion transport dynamics. Figure 2b exhibited the Nyquist plot comparison of various laminate graphene electrodes. 75% NHG-rGO electrode presents the smallest semicircle at high frequency region and nearly vertical straight line in the low frequency range, which indicates an ideal capacitive behavior and superior ion transport dynamics than other graphene electrode counterparts. We summarized fitted values of the specific equivalent circuit components in Table S3, Supporting Information, after a nonlinear least-squares fitting on the basis of the equivalent circuit exhibited in inset image of Figure 2b. Generally, 75% NHG-rGO electrode manifests remarkably inferior internal resistance (R_s) of

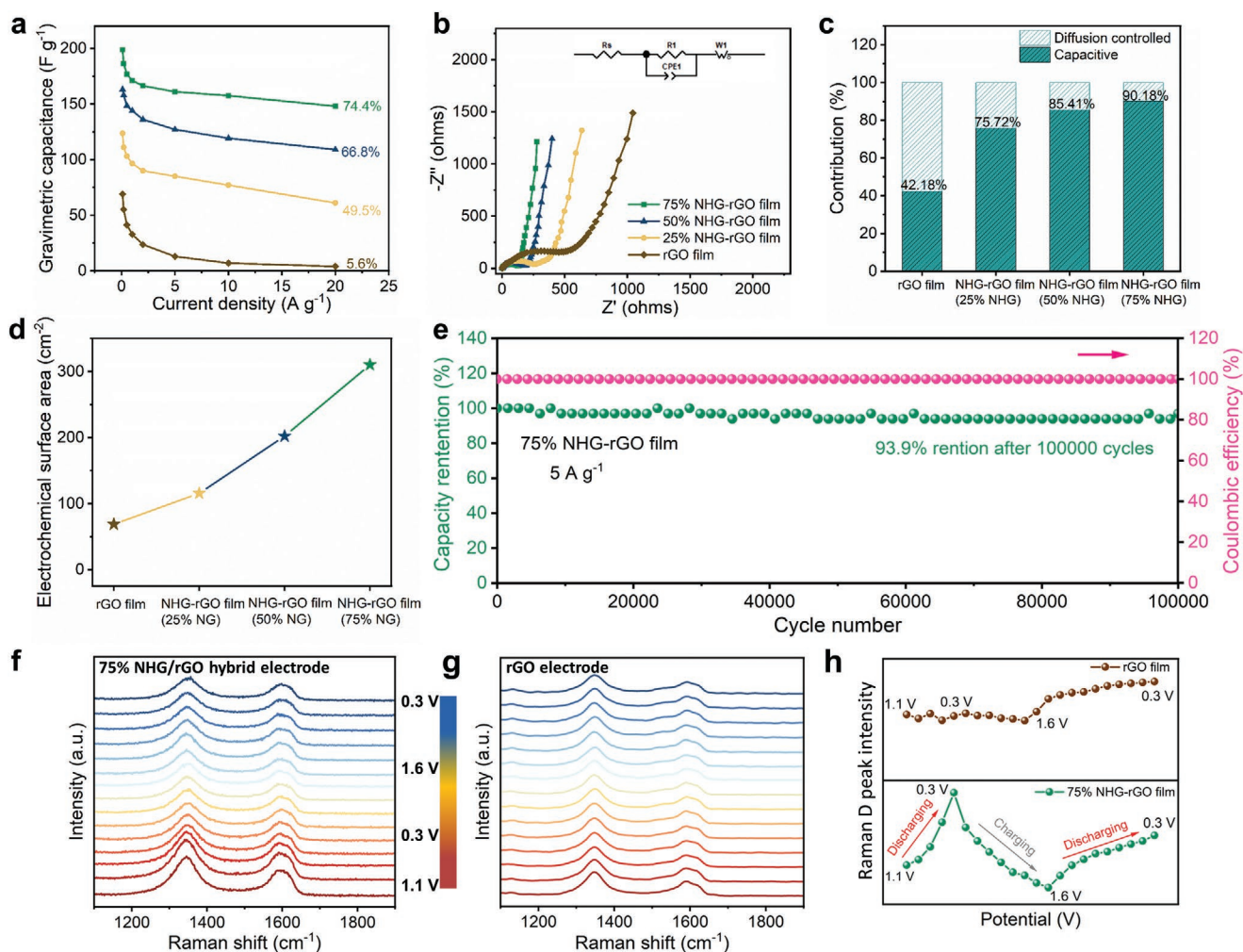


Figure 2. a) Gravimetric capacitance and rate performance at different current densities. b) Nyquist plots. c) Capacitance contribution calculation from CV curves of 5 mV s^{-1} . d) Differentiation of electrochemical specific area (ECSA). e) Cycling stability of 75% NHG-rGO film-based Zn-ion hybrid capacitor at current density of 5 A g^{-1} . f,g) In situ electrochemical Raman spectra of 75% NHG/rGO film hybrid electrode and rGO film electrode. h) Variation of intensity of D peak relative to potential.

0.62 Ω and charge transfer resistance of 125.6 Ω than those of 50% NHG-rGO, 25% NHG-rGO hybrid, and rGO electrodes. Thus, the 75% NHG-rGO hybrid electrode demonstrates more favorable electron conductivity and ion transport feature than any other graphene electrode counterparts.

Subsequently, as illustrated in Figure S11, Supporting Information, a universal complex model of the capacitance was applied to investigate the capacitance variations within a wide frequency, in which the real capacitance and imaginary capacitance were extracted from former EIS data. The time constant (τ_0) is defined as $\tau_0 = 1/f$ (f refers to the peak value of imaginary capacitance), which symbolizes the time required for releasing electric energy. The time constant (τ_0) values of these graphene electrodes were calculated as 16, 20, 25, and 50 s for 75% NHG-rGO film, 50% NHG-rGO film, 25% NHG-rGO film, and rGO film, respectively. The thus-obtained τ_0 for 75% NHG-rGO electrode suppressed the typical value of other reported graphene or porous carbon electrodes,^[11,38] which suggests great Zn ion transport dynamics even in such limited slit laminate channels.

Electrochemical capacity of hybrid capacitor could be generally categorized into capacitive charge storage and diffusion-controlled charge storage, in which the capacitive behavior delivers more efficient electrochemical kinetics at electrode/electrolyte interface and superior long-term cycling stability. Thus, we performed capacitance differentiation analysis based on CV curves with a series of systematic scan rates (Figure S12, Supporting Information). As summarized in Figure 2c, 75% NHG-rGO film electrode exhibited a considerable capacitive contribution of 90.18% at 5 mV s⁻¹, which is in good accordance with its good rate capability and great interfacial electrochemical kinetics.

Electrochemically active surface area (ECSA) is an effective indicator to represent the actual active surface area of graphene electrode that is accessible to Zn-ions. In contrast to BET surface area, it could be a more accurate index to evaluate the active surface that participates in Zn-ion adsorption charge storage process. ECSA of the series of graphene electrodes has been estimated through measuring CV curves with different scan rates in non-Faradic voltage region of 0.2–0.3 V (Figures S13 and S14, Supporting Information). As summarized in Figure 2d, 75% NHG-rGO electrode exhibited highest ECSA of 310 cm² which is far suppressed that of 50% NHG-rGO (202 cm²), 25% NHG-rGO (115 cm²), and rGO film (68 cm²) with limited interplanar channels.

By virtue of the capacitive charge storage mechanism and efficient ion transport dynamics originated from providential interlayer spacing, the 75% NHG-rGO film electrode exhibited an ultrahigh cycling stability with 93.9% capacity retention after 100 000 charge/discharge cycles at a current density of 5 A g⁻¹ (Figure 2e). To our best knowledge, this is an unprecedented cycling performance which outperforms all previously reported ZIHC so far (Table S4, Supporting Information). In contrast, 25% NHG-rGO film and rGO film electrode exhibited much poor cycling life, with capacitance retention of 86.95% and 66.67% after 50 000 cycles with the consistent current density (Figure S15, Supporting Information), respectively, which is hindered by moderate Zn ion migration in narrow laminate channels with limited ion diffusion efficiency.

In order to fully clarify the essence of the Zn-ion storage electrochemical behavior for interlayer spacing varied laminate graphene electrode, we performed *in operando* Raman spectroscopy to monitor the Zn-ion/graphene electrode interaction status during the Zn-ion adsorption/desorption. Figure 2f,g displayed the selected Raman spectra of 75% NHG-rGO hybrid and rGO electrodes during the real-time examination, in which the Raman spectra were collected during the electrode charging from open circuit voltage (OCP \approx 1.1 V) to 0.3 V, followed by an integral charging and discharging process between 0.3 and 1.6 V. The main peaks observed are D and G bands, appearing at 1345 and 1592 cm⁻¹, respectively. The D band is assigned to the intrinsic motion of sp² carbon atoms in the six-membered ring of crystalline graphene flakes. In comparison, G band is originated from the breathing motion of carbon atoms in the ring edges and defects in the graphene sheets. As referred from the previous literature, the physically adsorption of electrolyte ions on graphene flakes also performed as an electron-acceptor dopant-induced defect to represent the Zn-ion adsorption perturbation on graphene flakes.^[39] Thus, in this regard, the intensity of D bands I(D) summarized in Figure 2h, could serve as a typical indicator to identify the variation of Zn-ion adsorption/desorption onto the laminate graphene electrodes during the electrochemical process. The I(D) of 75% NHG-rGO hybrid electrode presents reversible enhancement during the applied voltage decrease to 0.3 V and gradual decrease while voltage approaches 1.6 V, which is in great accordance with the Zn-ion electrochemical adsorption/desorption. In sharp contrast, the rGO electrode with significantly contracted laminar spacing experienced a feeble intensity enhancement only while voltage exceeds 1.4 V. It implies that the Zn-ion adsorption into the rGO electrode has to conquer extra specific desolvation energy barrier for permeating into the slit laminated pores, which is the dominating factor for determining the limited electrolyte ion accessibility and inferior ion transport dynamics.

In addition to interlayer spacing of the laminate graphene electrode, the solvation structure of the Zn-ion is another critical prerequisite for optimizing the volumetric performance and correspondent rate or cycling stability. The electrolyte anions could also have specific influence on the solvation shell of Zn-ion hydration cluster. The typical size of hexahydrate Zn-ion [Zn(H₂O)₆]²⁺ in ZnSO₄ aqueous electrolyte, 0.86 nm, still exceed the average interlayer spacing (0.81 nm) of 75% NHG-rGO hybrid electrode, where the Zn-ion solvation shell still need slight distortion for inserting into the slit pores. Thus, we expect to rationally design the solvation shell of Zn-ion to coordinate with the specific interlayer spacing of 75% NHG-rGO hybrid electrode. We first scrutinize a series of Zn-ion electrolytes, namely ZnCl₂, Zn(Ac)₂, and Zn(CF₃SO₃)₂ in consistent 2 M concentration and 75% NHG-rGO hybrid electrode to benchmark the anion effects on the volumetric performance in comparison with ZnSO₄ for ZIHCs (Figure S16, Supporting Information). As depicted in Figure 3a, in ZnCl₂ aqueous electrolyte, ZIHC exhibited the highest volumetric capacitance of 235.4 F cm⁻³ (0.1 A g⁻¹) and optimal rate capability of 75.3% capacitance retention while current density increased to 20 A g⁻¹, which outperformed 202.7, 200.1, and 171.3 F cm⁻³ volumetric capacitance of ZnSO₄, Zn(Ac)₂, and Zn(CF₃SO₃)₂ systems, respectively. As summarized in Figure S17 and

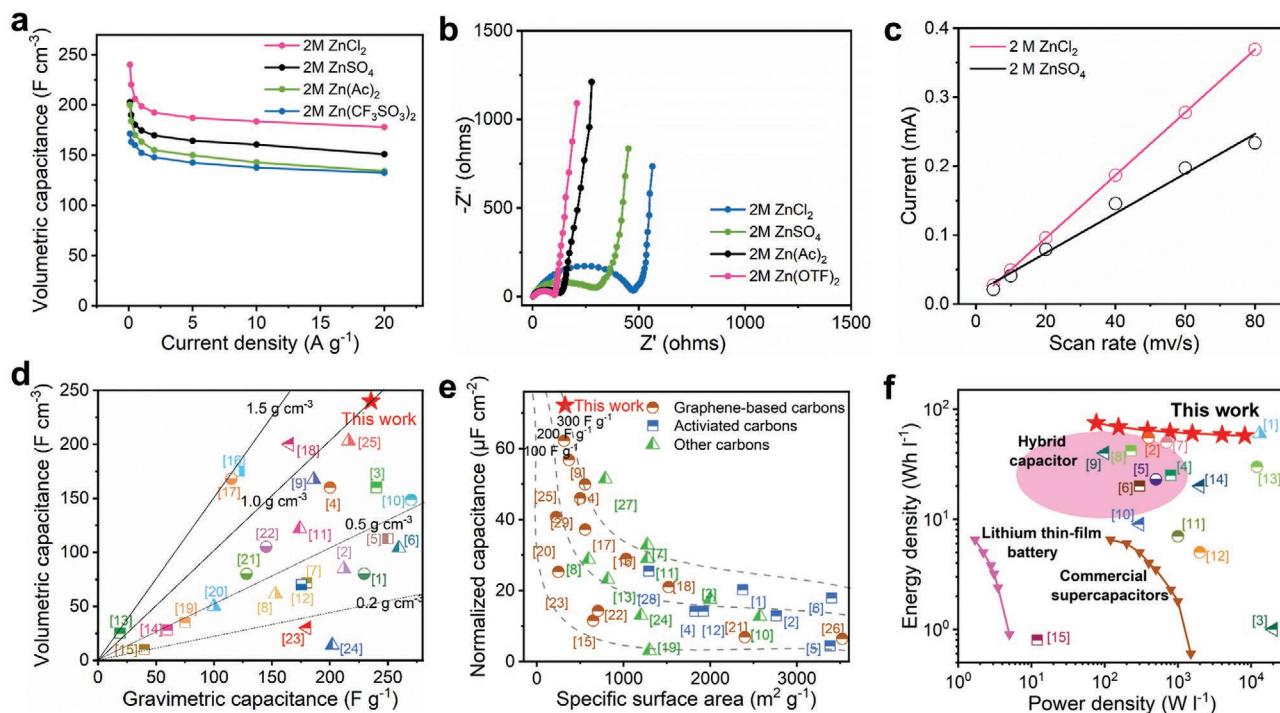


Figure 3. a) Volumetric capacitance at different current densities. b) Anodic charging currents measured at 0.25 V as a function of scan rate. c) Nyquist plots of 75% NHG/rGO film in varied electrolytes for comparison. d) Gravimetric and volumetric capacitance of 75% NHG/rGO film compared with reported electrode materials.^[32,40,41,44–65] e) Capacitance contribution per surface area of 75% NHG/rGO film in 2 M ZnCl₂ compared with other carbon materials.^[24,38,40,44–47,49,51–53,59,65,42,66–68] f) Ragone plot of volumetric energy density versus power density of 75% NHG/rGO film-based ZIHC compared with other aqueous hybrid capacitors, commercial supercapacitors, and lithium-film battery.^[22,59,65,66,69–74]

Table S5, Supporting Information, ZnCl₂ electrolyte-based ZIHC presents the best charge transfer efficiency, the fastest ion diffusion kinetics (Figure 3b) and lowest time constant (τ_0) value (10 s) among these investigated systems. Simultaneously, the ZnCl₂ electrolyte also peculiarly broadens the stable electrochemical voltage window to 0.2–1.7 V, which will be further elaborated in the following discussion. ECSA also has been investigated in ZnCl₂ electrolyte, in which 417 cm² ECSA suppressed the counterpart of ZIHC in ZnSO₄ (Figure 3c and Figure S18, Supporting Information). By virtue of the promoted ion transport kinetics and ECSA, ZIHC in ZnCl₂ electrolyte exhibited higher proportion of capacitive capacity contribution than that in ZnSO₄ (Figure S19, Supporting Information). Encouragingly, it exhibited extraordinary rate capability up to 100 A g⁻¹ with 66.7% capacity retention (Table S6, Supporting Information), which is one of the best rate performance even compared with all other reported ZIHCs.^[11,38,40–43]

Figure 3d demonstrated the comparison of specific capacitance and volumetric capacitance for thus-optimized 75% NHG-rGO electrode/ZnCl₂ system with other literatures also focusing on carbon-based ZIHCs and supercapacitors, such as GO-derived aMEGO which owns 80 000 cycles lifespan^[41] and liquid-mediated rGO films^[59] that realizes controllable density; nevertheless, they only delivered 84.8 and 200 F cm⁻³, respectively. In cooperation with the rational selection of Zn-ion electrolyte salt, the optimal design of the densely packing 75% NHG-rGO electrode reached an exceptional volumetric and gravimetric performance compared with most

previously reported carbon-based ZIHCs and even supercapacitors.^[32,40,41,44–65] To further specify the superiority of optimized space utilization for thus-customized graphene lamellar electrode/electrolyte unit, we calculated the specific areal capacitance based on the specific area of the porous carbon, that is, C_{ssa} . As summarized in Figure 3e, the obtained C_{ssa} of 72 μF cm⁻² outperformed all previously reported capacitors based on carbon electrodes, such as graphene, activated carbons, and other porous carbon (e.g., templated carbon and carbide-derived carbon).^[24,38,40,44–47,49,51–53,59,65,42,66–68] For instance, holy graphene framework derived through KOH activation only presented 28.9 μF cm⁻²,^[66] even though EG-mediated rGO film with abundant narrow spaces just delivered 46 μF cm⁻²,^[32] which is further demonstrating the outstanding space utilization ratio.

With the combination of distinguished volumetric capacitance, and extended voltage range, thus-fabricated ZIHC composed of 75% NHG-rGO film immersed in ZnCl₂ electrolyte could deliver a remarkable energy density of 75 W h l⁻¹ (73.6 W h kg⁻¹) at power density of 76.7 W l⁻¹ (75.2 W kg⁻¹) which is even comparable to some state-of-the-art aqueous hybrid capacitors, and commercial supercapacitors (Figure 3f).^[22,59,65,66,69–74] In addition, the resultant ZIHC also demonstrates an excellent cycling performance with a capacitance retention of 94.05% after 40 000 charging/discharging cycles (Figure S20, Supporting Information).

Switching with ZnCl₂ significantly promoted the volumetric capacitance by maximizing the spacing utilization of

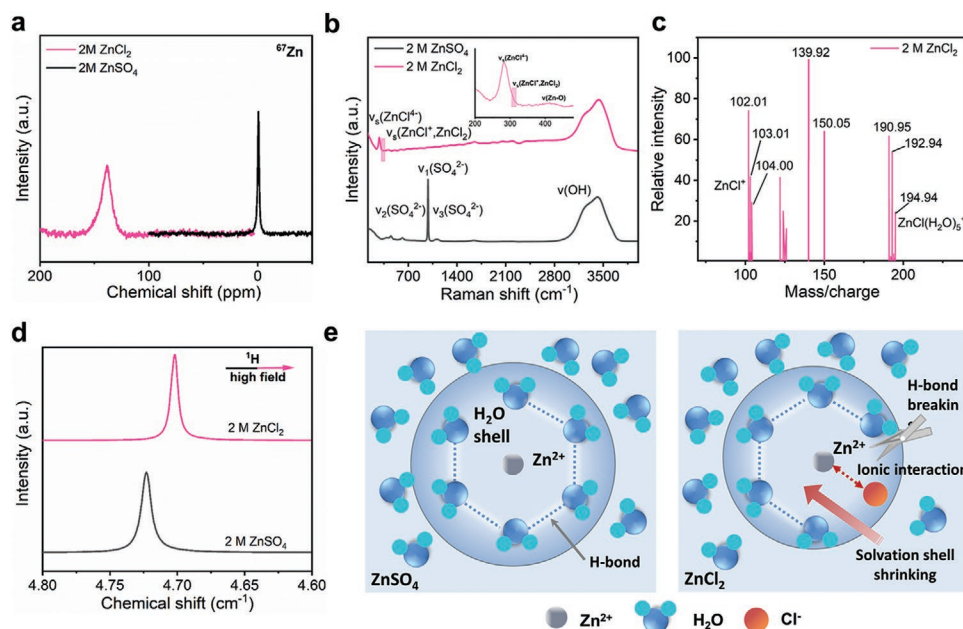


Figure 4. Spectroscopy characterization of the solvation structure of ZnSO_4 and ZnCl_2 electrolytes. a) ^{67}Zn NMR spectra in ZnSO_4 and ZnCl_2 electrolytes. b) Raman spectra of ZnSO_4 and ZnCl_2 aqueous solution. c) Ionic high resolution mass spectra (HRMS) of ZnCl_2 aqueous electrolyte, demonstrating the presence of a number of hydrated Zn-ion complexes $[\text{Zn}(\text{H}_2\text{O})_5\text{Cl}]^+$ ($m/z = 191, 193, 195$). d) ^1H NMR spectra of ZnSO_4 and ZnCl_2 aqueous electrolytes. e) Schematic diagram of Zn^{2+} solvation structure in ZnSO_4 and ZnCl_2 electrolytes, respectively.

the consistent as-fabricated laminate graphene electrode in contrast to other Zn-ion salt systems, hence, we deduced that ZnCl_2 aqueous solution should manifest a unique solvation shell structure, thereby facilitating the more efficient Zn-ion storage in 75% NHG-rGO electrode. In general, the solvation structure is mostly determined by the first shell close to naked Zn^{2+} , which mainly quantitatively described by the amount of strong bonding between Zn^{2+} and H_2O . In order to precisely describe the chemical environment difference of solvation structure of ZnSO_4 and ZnCl_2 solution, we conducted a series of spectra characterizations, including ^{67}Zn , ^1H , NMR spectroscopy, Raman, and ionic high-resolution mass spectra (HRMS). As exhibited in Figure 4a, ^{67}Zn NMR spectroscopy demonstrated that ZnCl_2 aqueous electrolyte presents a conspicuously chemical shift (138 ppm) deviation compared with that of ZnSO_4 electrolyte (-0.7 ppm), indicating the representative deshielding effect of solvation shell containing Cl^- on Zn ions. It could be contributed by Cl^- introduction triggered solvation structure variation via forming Zn–Cl ionic linking complex. In this regard, Raman spectra have been performed to probe the specific Zn^{2+} complex structure in both of ZnCl_2 and ZnSO_4 aqueous solutions. As depicted in Figure 4b, Raman spectra of ZnCl_2 aqueous electrolyte presents a prominent peak located at 283 cm^{-1} and a side peak appeared at 310 cm^{-1} , which could be assigned to the symmetric stretching modes of the tetrahedral $[\text{ZnCl}_4]^{2-}$ and $[\text{ZnCl}]^+$ species,^[40] respectively, which further verifies the Zn–Cl complex formation in ZnCl_2 electrolyte. In contrast, there are no other indicative peaks in Raman spectra of ZnSO_4 electrolyte, in addition to the typical peaks at $452, 983$, and 1117 cm^{-1} arising from symmetric stretching modes of SO_4^{2-} group.

Furthermore, the broad peak centered at 3400 cm^{-1} is assigned to O–H stretching vibration of H_2O (Figure 4b),

which is often convolved into H_2O with strong H-bond, weak H-bond, and none H-bond, respectively.^[75] As summarized in Figure S21, Supporting Information, in contrast to the 40.52% of strong H-bond in Raman for ZnSO_4 solution, ZnCl_2 electrolyte exhibited the obviously depressed proportion (36.69%), indicating the durative destruction of H-bond structure with the introduction of Cl^- . Benefiting from the destruction of H-bond structure in aqueous solution by Cl^- , the activity of free H_2O molecular is reduced and H_2O decomposition is also prevented. This result sufficiently explains that why ZnCl_2 electrolyte has a broader voltage window than ZnSO_4 electrolyte, as mentioned in the electrochemical results above. HRMS is evidenced as a powerful technique in analysis of electrolyte solvation structure.^[76] As depicted in Figure 4c, we could observe a series of distinct peaks for Zn–Cl associated species, such as $[102, 103, 104]$ and $[191, 193, 195]$, which could be assigned to ZnCl^+ and $[\text{Zn}(\text{H}_2\text{O})_5\text{Cl}]^+$, respectively. The different peak positions of mass spectra for a single complex, such as ZnCl^+ and $[\text{Zn}(\text{H}_2\text{O})_5\text{Cl}]^+$ are attributed to the presence of Zn and Cl isotopes. ^1H NMR results also verified this point where ^1H chemical shift of ZnCl_2 solution moved to higher magnetic field than that of ZnSO_4 (Figure 4d), which means weakening the bonding strength between Zn^{2+} and hydration sheath. Thus, the series of spectra characterization systematically confirmed that the Zn–Cl bonding partially replace the H_2O molecular at the first shell of solvation Zn^{2+} . As schematically illustrated in Figure 4e, due to disturbance of the Cl^- bonding with stronger binding energy, the size of Zn^{2+} solvation sheath tends to subsequently shrink via the preferential solvation of Cl^- .

Ab initio molecular dynamics (AIMD) simulations were performed to simulate the solvation structure of 2 M ZnSO_4 and ZnCl_2 aqueous electrolytes, to investigate the detailed

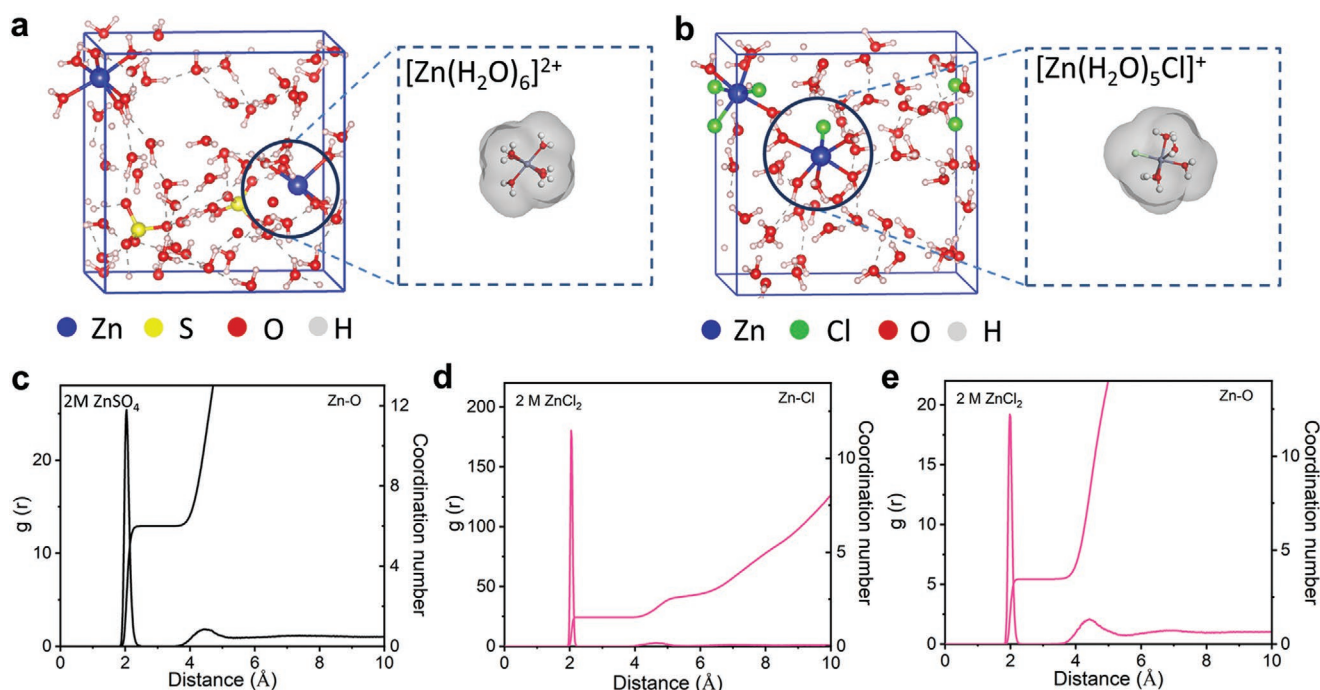


Figure 5. a,b) AIMD snapshot of ZnSO₄ electrolyte and ZnCl₂ electrolyte; local enlarged snapshot represents Zn²⁺ solvation structure, respectively. c) The radial distribution function (RDF) and coordination number for Zn–O in ZnSO₄ electrolyte. d) RDF and coordination number for Zn–Cl and e) Zn–O in ZnCl₂ electrolyte summarized from MD simulations.

coordination environment. In ZnSO₄ system, the simulation results demonstrates that the primary solvation shell consists of six H₂O molecules around Zn²⁺ when the system reaches equilibrium (Figure 5a). In contrast, in a AIMD simulation starting with Zn(H₂O)₆²⁺, Cl[−] can automatically replace one H₂O in the first solvation shell to form [Zn(H₂O)₅Cl]⁺ (Figure 5b). Such spontaneous process indicates that Cl[−] is prone to enter the primary solvation shell. Although free energy calculations are required to access the precise free energy differences between Zn(H₂O)₆²⁺ and [Zn(H₂O)₅Cl]⁺, above calculations already demonstrate that [Zn(H₂O)₅Cl]⁺ is stable and can exist in the designed electrolyte. Corresponding pair radial distribution functions $g_{ab}(r)$ from AIMD simulations were calculated to show specific coordination numbers of two thus-prepared electrolyte systems in Figure 5a,b. In 2 M ZnSO₄ electrolyte, a sharp peak of Zn–O bond located at around 2.1 Å away from Zn²⁺ should be attributed to the H₂O molecules inside primary solvation shell of Zn²⁺ (Figure 5c). No obvious peak of Zn–S coordination is observed (Figure S22, Supporting Information), which is in consistent with Raman analysis presented in Figure 4b. Instead, a distinct peak originated from Zn–Cl bond appears at around 2.2 Å, which demonstrates the presence of Zn–Cl interaction in the primitive solvation shell (Figure 5d). The integrated Zn²⁺–H₂O coordination number in primary hydration shell of ZnSO₄ and ZnCl₂ electrolytes are 6 and 4.5, respectively (right axis of Figure 5c,e). Meanwhile, the average coordination number of Zn–Cl in first hydration layer within ZnCl₂ electrolyte is ≈1 (right axis of Figure 5d). These simulation results further confirm that the presence of Cl[−] uniquely leads to the formation of Zn²⁺–Cl[−] clusters, among which [Zn(H₂O)₅Cl]⁺ would directly correlate to the ion storage in ZIHCs because

of its positive charge and high abundance. In addition, the presence of Cl[−] ions have been proved to facilitate the desolvation of [Zn(H₂O)₅Cl]⁺, which subsequently enables the more efficient charge storage in narrow porous carbon electrodes.^[40] Hydrogen bonding (HB) was determined by taking a criteria of O–O distance cut-off of 3.5 Å, and a O–H–O angle cut-off of 30°. AIMD simulation indicates that with same amount of water molecules, the ZnCl₂ model has 535 HB, which is less than that of 656 of its counterpart, in ZnSO₄, indicating that Cl[−] is beneficial for breaking HB network surrounding Zn²⁺. The formation of [Zn(H₂O)₅Cl]⁺ solvation shell and significantly reduced HBs in ZnCl₂ electrolyte are fully agreed with the NMR, Raman, and HRMS analysis results in the previous section. The contracted size of electrolyte ions, smaller than inter-layer spacing in the laminate graphene sheet, is responsible for the creation of such a noticeable space utilization ratio. Therefore, the significantly improved performance of thus-prepared ZIHCs can be explained as the introduction of Cl[−] that modifies Zn²⁺ solvation structure leading to the dominant presence of [Zn(H₂O)₅Cl]⁺.

In order to demonstrate the realistic application scenario of such coupled laminate graphene electrode and ZnCl₂ electrolyte, we assembled a quasi-solid-state ZIHC composed of 75% NHG-rGO film as cathode and PAM/ZnCl₂ hydrogel as electrolyte. Figure 6a demonstrated the schematic diagram of the quasi-solid-state ZIHC configuration and integrated wearable application. The thus-assembled quasi-solid-state ZIHC could be directly utilized as a flexible power supply element for electronic watch, which exhibits a remarkable areal capacitance of 1227 mF cm^{−2} with an active material loading mass of 6 mg cm^{−2} (Figure 6b). It is still able to deliver

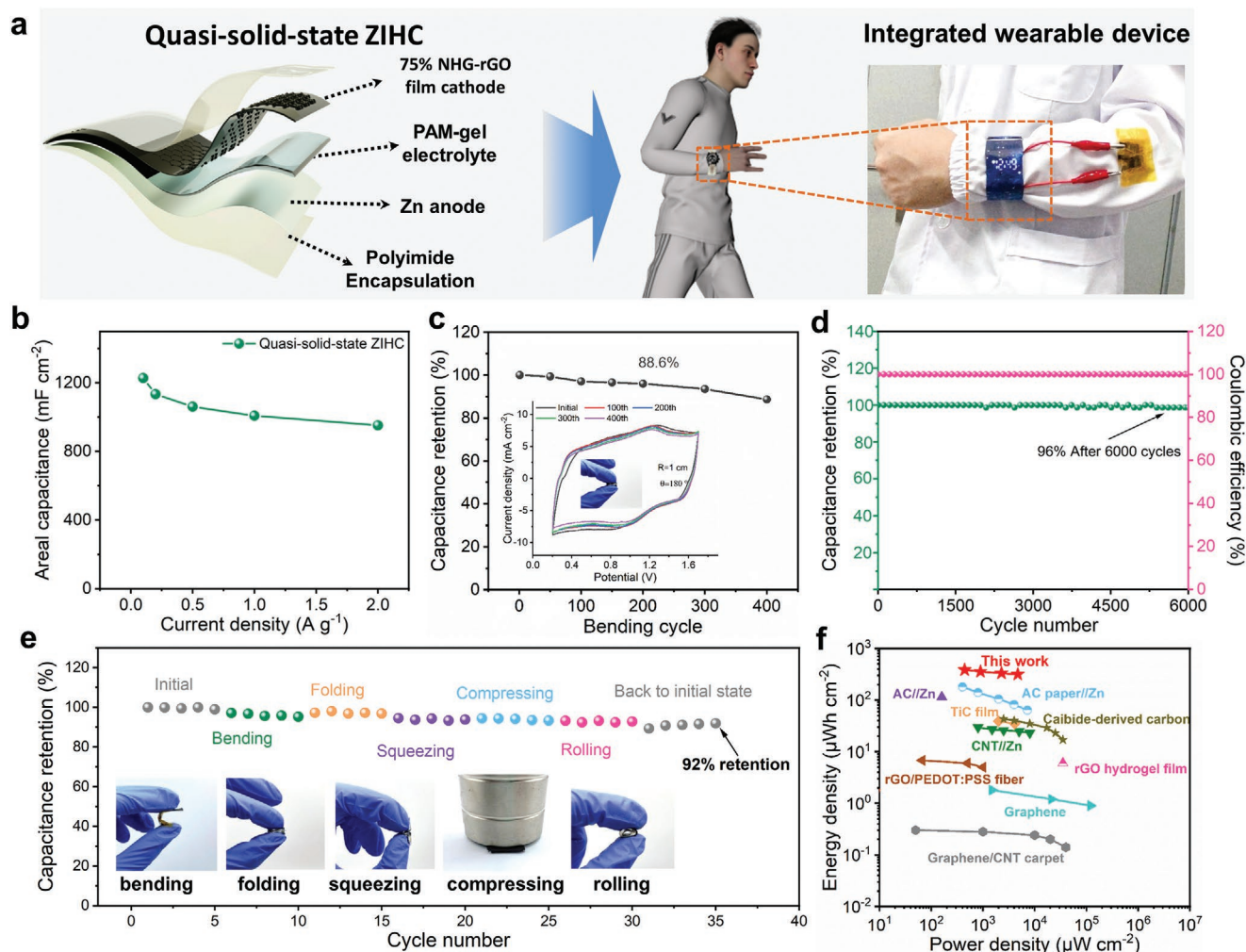


Figure 6. Display and corresponding performance of flexible ZIHC based on 75% NHG-rGO film in ZnCl_2 electrolyte. a) Schematic diagram and wearable display of the quasi-solid-state ZIHC. b) Areal capacitance of as-fabricated quasi-solid-state ZIHC at varied current densities. c) Capacitance retention of the as-fabricated ZIHC under bending condition. Inset is the corresponding CV curves at certain intervals. d) Cycling performance and Coulombic efficiency of the quasi-solid-state ZIHC. e) Capacitance retention of the quasi-solid-state ZIHC obtained from GCD curves under different mechanical stimulation. f) Ragone plot of as-fabricated ZIHC compared with recent reported ZIHCs and other aqueous hybrid capacitors.^[11,22,53,77–80]

952 mF cm^{-2} even as current density increases to 2 A g^{-1} . The as-prepared ZIHC also displays excellent mechanical flexibility, even the folded thickness approaching 1.5 mm (Figure S23, Supporting Information). As depicted in Figure S24, Supporting Information, there is no obvious capacity fluctuation when bending angle increase from 0° to 90° with 3 cm device length and 1 cm curvature radius. We also characterized the flexibility cycling stability by examining the capacitance retention of quasi-solid-state ZIHC while bending the device with bending angle (θ) of 180° and curvature radius (R) of 1 cm for 400 cycles. As displayed in Figure 6c, the thus-assembled quasi-solid-state ZIHC presents negligible capacitance loss at first 50 times bending and still retains 88.6% even bending 400 times, implying the excellent electrochemical stability and mechanical property. Afterward, the long cycling test of the quasi-solid-state ZIHC was performed to evaluate its cycling stability, which indicates 96% capacity retention even after 6000 cycles and nearly 100% Coulombic efficiency (Figure 6d). In addition, long cyclic tests

were performed under various mechanical impacts including bending, folding, squeezing, compressing, and rolling, respectively, as depicted in Figure 6e, which manifest about 92% capacity retention after 35 cycles of device configuration deformation, further confirming the exceptional stability and durability of ZIHC under various mechanical impacts. Benefit from the excellent properties of graphene films, the quasi-solid-state 75% NHG-rGO//Zn ZIHC exhibited an superior areal energy density of $383 \mu\text{Wh cm}^{-2}$ at $442 \mu\text{W cm}^{-2}$, which far outstripped recent reported aqueous ZIHCs, such as Zn//CNT ZIHC ($29.6 \mu\text{Wh cm}^{-2}$),^[77] as summarized in Ragone plot in Figure 6f and Table S7, Supporting Information.^[11,22,53,77–80]

3. Conclusion

In summary, we constructed an aqueous ZIHC by harmonizing interlayer spacing of laminate graphene film and Zn-ion

solvation structure to achieve compact electrolyte ion storage in limited device space. In coupling of laminate graphene inter-spacing optimization and Zn-ion solvation structure regulation, the thus-assembled ZIHC manifests a superior cycling life of 100 000 cycles with 93.9% capacitance retention and an outstanding volumetric capacitance of 235.4 F cm^{-3} . Specifically, experimental results and computational modeling together verified that solvation structure of the unique ZnCl_2 electrolyte could remarkably improve the Zn-ion accessibility. Furthermore, the flexible quasi-solid-state ZIHC based on 75% NHG-rGO film with PAM gel delivers a remarkable areal capacitance of 1227 mF cm^{-2} and excellent mechanical flexibility of 88.6% capacity retention after 400 cycles even under repeatedly folding cycles. The performance enhancement of optimized ZIHC further emphasizes the importance of accoupling effect of ion solvation structure and pore architecture on the performance in Zn-ion energy storage.

4. Experimental Section

Preparation of Graphene Oxide: Graphene oxide was prepared from natural graphite flakes by the modified Hummer's method.^[59] Briefly, graphite powder (2 g) was added into H_2SO_4 (46 mL) under continuous stirring at 0°C . Then, KMnO_4 (6 g) was added into the mixed solutions under uniformly stirring in an ice bath. After stirring for 1 h, the mixture was heated at 30°C for 1 h. Deionized water (69 mL) was further slowly added into the solution in the process of heating up to 96°C , and keeping for 30 min. Finally, H_2O_2 (20 mL) and water (210 mL) was added into the mixture to terminate the reaction, and in this process, the color changes from earthy yellow to bright yellow. The product was washed using dilute HCl (5%) through centrifuging three times, followed by washing with ethanol until neutral. The GO powder was collected by freeze-drying.

Preparation of NHG: The preparation of NHG was based on the previous research of chemically converted graphene sheets.^[59] In detail, 41 μL hydrazine hydrate (85 wt%) and 700 μL ammonia (28 wt%) were added into 250 mL 0.2 mg mL^{-1} GO dispersion. Then the mixed solutions were heated at 100°C for 3 h to reduce the GO flakes adequately.

Preparation of NHG-rGO Films: NHG-rGO hybrid films were prepared by vacuum filtration of the dispersions of NHG and GO in a certain mass ratio. Using NHG-rGO (50% NHG) for an example, GO solution ($20 \text{ mL } 0.2 \text{ mg mL}^{-1}$) and NHG solution ($20 \text{ mL } 0.2 \text{ mg mL}^{-1}$) were mixed under stirring for 2 min. Then the homogenous dispersion was filtered through a cellulose membrane ($0.2 \mu\text{m}$). The NHG-rGO films were then carefully peeled off from the filter membrane, followed by soaking into HI solution (55 wt%) for 1 h to enhance the conductivity of hybrid films. The ultimate NHG-rGO films were repeatedly washed with ethanol and deionized water for five times to remove the redundant HI. As a contrast, NHG and rGO films were prepared with the same method but from pure GO and NHG dispersions, respectively. The areal mass loading of as-obtained NHG-rGO films was $\approx 0.66 \text{ mg cm}^{-2}$.

Fabrication of Zn-ion Hybrid Capacitors: ZIHC was fabricated in a symmetric two-electrode configuration to assess the electrochemical performance. Before the assembly of Zn-ion hybrid capacitor, NHG-rGO films were cut into $1 \text{ cm} \times 1 \text{ cm}$ square pieces and then soaked into 2 M ZnSO_4 and 2 M ZnCl_2 overnight to exchange internal water with electrolyte. Subsequently, NHG-rGO films were placed onto titanium foils as working electrode. Zn foil was used as anode electrode, which was punched into 13 mm diameter. Two electrodes with a glass fiber separator ($\phi = 19 \text{ mm}$) were assembled into a sandwich-like structure in the form of CR2032 coin-cell with electrolyte.

Assembly of Flexible Quasi-Solid-State Zn-ion Hybrid Capacitor: The Zn//PAM//NHG-rGO quasi-solid state ZIHCs were fabricated by

using Zn foil as anode, NHG-rGO film electrode as cathode, and PAM/ ZnCl_2 as gel electrolyte, respectively. Then the whole device was encapsulated by polyimide type, followed by removing the excess air.

PAM gel was prepared on the basis of the previously reported methods.^[17] First, 3 g starch was fully dissolved in 30 mL deionized water, then mixed uniformly with heating at 100°C for 1 h. Afterwards, 30 mg $(\text{NH}_4)_2\text{S}_2\text{O}_8$, 5 g acrylamide monomer, and 3 mg of N,N' -methylene bisacrylamide were slowly added into the above solution under continuous stirring. Then the solution was poured into a mould with a thickness of 1 mm and dried at 80°C for 2 h. Ultimately the peeled PAM gel was immersed into 2 M ZnCl_2 for 1 day to adsorb the electrolyte sufficiently.

Electrochemical Measurement: All electrochemical experiments were carried out on a Princeton workstation at room temperature (25°C). The stable working window of ZIHCs was evaluated using a three-electrode configuration, which used a Zn foil as counter electrode, a Ag/AgCl electrode as reference electrode, a $1 \text{ cm} \times 1 \text{ cm}$ NHG-rGO film as working electrode. CV and GCD tests were operated at different scan rates and current densities. The EIS tests were operated at the open circuit voltage with an amplitude voltage of 5 mV in the frequency range from 1 MHz to 10 mHz. The evaluation of cycling life was realized through continuous GCD cycles at a current density of 5 A g^{-1} by the Neware battery testing system (CT-4008T).

The specific gravimetric capacitance (C_{wt} , F g^{-1}) based on film electrode was derived from GCD curves using the following Equation (1):

$$C_{\text{wt}} = \frac{It}{mU} \quad (1)$$

where I was applied current (A), t was the discharging time, m was the mass loading of NHG-rGO films, and U was the voltage window with excluding the IR drop (V).

The corresponding volumetric specific capacitance (C_{vol} , F cm^{-3}) was calculated according to the Equation (2):

$$C_{\text{vol}} = C_{\text{wt}} \times \rho \quad (2)$$

where ρ was the density of electrode material (g cm^{-3}) and C_{wt} was specific capacitance of electrode (F g^{-1}).

The volumetric energy density (E_{vol} , Wh L^{-1}) and volumetric power density (P_{vol} , W L^{-1}) of ZIHCs were calculated from the following Equations (3) and (4):

$$E_{\text{vol}} = \frac{1}{2 \times 3.6} C_{\text{vol}} \times V^2 \quad (3)$$

$$P_{\text{vol}} = \frac{E_{\text{vol}}}{t} \times 3600 \quad (4)$$

where C_{vol} was the specific volumetric capacitance of film electrode (F cm^{-3}), V was the working voltage window (V), and t was the discharge time (h).

The areal energy density (E_{a} , Wh cm^{-2}) and areal power density (P_{a} , W cm^{-2}) of ZIHCs were calculated from the following Equations (5) and (6):

$$E_{\text{a}} = \frac{1}{2 \times 3.6} C_{\text{a}} \times V^2 \quad (5)$$

$$P_{\text{a}} = \frac{E_{\text{a}}}{t} \times 3600 \quad (6)$$

where C_{a} was the areal capacitance (F cm^{-2}), V was the potential window (V), and t was discharge time (h).

Quantitative capacitance differentiation was performed on CV curves, using the following Equation (7):

$$i(\nu) = k_1\nu + k_2\nu^{1/2} \quad (7)$$

where $i(\nu)$ was the current density response at a fixed voltage, k_1 was the capacitive effect factor, k_2 was the diffusion process effect factor, and ν was the scan rate.

ECSA was calculated by the following Equations (8) and (9):

$$i_c = C_{dl} \frac{d\phi}{dt} \quad (8)$$

$$ECSA = \frac{C_{dl}}{C_{dl(smooth)}} \quad (9)$$

where C_{dl} was the electrochemical double layer capacitance, i_c was the current density, $d\phi/dt$ was scan rate, and $C_{dl(smooth)}$ was the double layer capacitance value of a smooth surface.

Physicochemical Characterization: XRD patterns were obtained from a Bruker D8 advanced diffractometer with Cu-K α radiation ($\lambda = 1.5406 \text{ \AA}$), and the data were collected from 3° to 40° with a scan rate of $10^\circ \text{ min}^{-1}$. The morphology and structure of the prepared films were collected by scanning electron microscopes (FEI Scios) with an accelerating voltage of 10.0 kV. The thickness of the prepared films were measured from the cross-sectional SEM images, and subsequently used to compute corresponding bulk density. X-ray photoelectron spectroscopy was collected through an ESCALAB 250Xi spectrophotometer using a monochromatic Al K α X-ray source (Thermo Fisher Scientific). The Fourier-transform infrared spectroscopy was carried out in an absorption mode (Bruker Tensor 27). The Raman spectroscopy was performed by using a LabRAM HR800 (Jobin Yvon) instrument with a 532 nm incident radiation and a 50 \times aperture. AFM images were obtained using a Bruker Dimension Icon Scanning Probe Microscope in tapping mode. N₂ adsorption-desorption isotherms (77 K) were measured using an ASAP 2460 instrument. Before analysis, the sample was heated at 160 $^\circ\text{C}$ under vacuum for 24 h to remove all possibly adsorbed species. The SSA of the sample was measured according to Brunauer-Emmett-Teller (BET) equation.

In Situ Electrochemical Raman Spectroscopy: As an effective characterization method to reflect the properties of graphene-based materials, Raman spectroscopy could reflect their characteristics including defects, doping, and number of layers. For a graphene-based material, its charge/discharge process was often accompanied by the intercalation and detachment of ions between the interlayer spaces. Here, in situ Raman was used to track electrochemical behaviors of electrolyte ions inside film electrodes. Briefly, the in situ Raman test was conducted by using electrode materials discharged ranging from open circuit voltage to 0.3 V and charged from 0.3 to 1.6 V; in the meantime, Raman spectroscopy was continuously recorded on the electrode materials.

Solid-State Nuclear Magnetic Resonance Spectroscopy: ^1H MAS-NMR experiment was performed on a Bruker Avance III HD 400WB spectrometer operating at a magnetic field strength of 9.4 T and 400.2 MHz for ^1H on a 3.2 mm CPMAS probe. Experiments of electrolyte adsorption were performed at 10 kHz spinning speed to avoid baseline distortions and further exclude background signals about the probe. ^1H NMR spectra of samples were referenced relative to tetramethylsilane at 0 ppm. The spin-lattice relaxation time (T_1) of ^1H was evaluated by inversion-recovery sequence in the condition of air. A recycle time of 2 s was used for ^1H experiments, found to give quantitative spectra. About the sample preparation, a graphene film piece (25 mg) was cut into small pieces and heated at 200 $^\circ\text{C}$ for 15 h. Before the test, 37.5 μL 2 m ZnSO_4 electrolyte was slowly added into a glass vial containing samples, and then stirred the electrolyte and sample evenly with a syringe needle. Finally, all samples were packed into a 3.5 mm outer diameter zirconia rotor for tests.

Molecular Dynamics Simulation: Simulation Model: To simulate 2 m ZnCl_2 , the system included 53 water molecules, 2 ZnCl_2 molecules in a 1.3 nm cubic simulation box. The initial structure was created by random insertion of molecules into the simulation box. To simulate 2 m ZnSO_4 , the system included 53 water molecules and 2 ZnSO_4 molecules in a 1.3 nm cubic simulation box. The initial structure was created by random insertion of molecules into the simulation box. The authors first performed geometry optimization by using DFT. From the obtained structure, a 10 ps AIMD calculations

was carried out. The solvation structures of $\text{Zn}(\text{H}_2\text{O})_6$, $\text{Zn}(\text{H}_2\text{O})_5\text{Cl}$, and $\text{Zn}(\text{H}_2\text{O})_4\text{Cl}_2$ were rendered by Gaussian View. In the molecular mechanics MD simulations, the authors expanded the simulation box by a factor of two in all three directions, so the total volume was expanded by a factor of eight.

Simulation Method: Density Functional Theory Simulation: The quantum mechanical calculations were performed using Vienna Ab initio Simulation Package at a version of 5.4.4 with the projector augmented wave method and a plane wave basis set. The method was DFT with generalized gradient approximations of Perdew-Burke-Ernzerhof functional.^[81] A dispersion correction, DFT-D3 method with Becke-Jonson damping,^[82] was included in the calculations. The energy cut-off was set to 400 eV. Larger energy cut-off did not produce more accurate prediction basing on the authors' benchmark calculation. Reciprocal space was sampled by Γ -centered Monkhorst-Pack scheme with a grid of $3 \times 3 \times 1$. Finer K spacing did not produce more accurate prediction basin on the authors' benchmark calculation. Spin polarization did not have an appreciable effect on the overall energies and was not included in the calculations to reduce computational demands. The partial occupancies for each orbital were set with the first order Methfessel-Paxton scheme in the smearing width of 0.2 eV. The dipole moment corrections for the total energy were considered in the direction normal to the surface. The self-consistent electronic step was considered converged when the change of total energy and eigenvalues changed between two steps were both smaller than 1e^{-5} eV.

A conjugate-gradient algorithm was used to relax the ions in energy minimization. The minimization was considered converged when all the atomic force was smaller than 0.02 eV \AA^{-1} .

Solvation structures were optimized by Gaussian 16 at a level of B3LYP with the 6-31G(d) basis set for all atoms. (M. J. Frisch, G. W. Trucks, H. B. Schlegel, G. E. Scuseria, M. A. Robb, J. R. Cheeseman, G. Scalmani, V. Barone, G. A. Petersson, H. Nakatsuji, X. Li, M. Caricato, A. V. Marenich, J. Bloino, B. G. Janesko, R. Gomperts, B. Mennucci, H. P. Hratchian, J. V. Ortiz, A. F. Izmaylov, J. L. Sonnenberg, D. Williams-Young, F. Ding, F. Lipparini, F. Egidi, J. Goings, B. Peng, A. Petrone, T. Henderson, D. Ranasinghe, V. G. Zakrzewski, J. Gao, N. Rega, G. Zheng, W. Liang, M. Hada, M. Ehara, K. Toyota, R. Fukuda, J. Hasegawa, M. Ishida, T. Nakajima, Y. Honda, O. Kitao, H. Nakai, T. Vreven, K. Throssell, J. A. Montgomery Jr., J. E. Peralta, F. Ogliaro, M. J. Bearpark, J. J. Heyd, E. N. Brothers, K. N. Kudin, V. N. Staroverov, T. A. Keith, R. Kobayashi, J. Normand, K. Raghavachari, A. P. Rendell, J. C. Burant, S. S. Iyengar, J. Tomasi, M. Cossi, J. M. Millam, M. Klene, C. Adamo, R. Cammi, J. W. Ochterski, R. L. Martin, K. Morokuma, O. Farkas, J. B. Foresman, D. J. Fox, Gaussian 16 (Revision A.03), Inc., Wallingford CT, 2016.)

The density functional theory-Molecular Dynamics (DFT-MD) simulations were performed in the canonical (NVT) ensembles. The authors used a 1 fs time step in the DFT-MD simulations. These DFT-MD simulations used only the gamma point of the Brillouin zone with no consideration of symmetry. For DFT-MD equilibrations, the velocities were scaled to the target temperature every 20 steps. For DFT-MD productions, the time integration was Nose-Hoover style non-Hamiltonian equations of motion with a timespan of 200 fs.

Molecular Mechanics-Molecular Dynamics Simulation: The force field of water molecules was modeled by SPC/E. In the initial force field, the charge of Zn cation was +2, and the van der Waals (vdW) parameter was from Universal force field (UFF). The charge of Cl anion was -1, and the vdW parameter was from UFF. The total charge of SO_4 anion was -2, and the vdW parameter was from UFF force field. The intramolecular parameters of SO_4 anion were obtained by fitting the results of DFT calculations. Based on the DFT-MD simulation results, the authors further adjusted the charge parameter and vdW parameters of the ions to reproduce the DFT calculations.

Supporting Information

Supporting Information is available from the Wiley Online Library or from the author.

Acknowledgements

J.R.L. and L.X. contributed equally to this work. This project was financially supported by: a start-up research grant for a distinguished professor at Soochow University Y.S. (Yuanlong), the National Natural Science Foundation of China No. 52003188 Y.S. (Yuanlong), No. 21903058 (T.C.), and 22173066 (T.C.), the Natural Science Foundation of Jiangsu Province No. BK20200871 Y.S. (Yuanlong) and No. BK20190810 (T.C.), Jiangsu Innovation and Entrepreneurship Talent Program (JSSCR2021529), open research fund for Jiangsu Provincial Key Laboratory for Advanced Carbon Materials and Wearable Energy Technologies Y.S. (Yuanlong), open research fund State Key Laboratory for Modification of Chemical Fibers and Polymer Materials, Donghua University No. KF2104 Y.S. (Yuanlong), Gusu's Young Leading Talent (ZXL2021449 (Y.S. (Yuanlong))), Key Industry Technology Innovation Project of Suzhou (SYG202108 (Y.S. (Yuanlong))), Collaborative Innovation Center of Suzhou Nano Science & Technology, the Priority Academic Program Development of Jiangsu Higher Education Institutions (PAPD), and the 111 Project, Joint International Research Laboratory of Carbon-Based Functional Materials and Devices (T.C.).

Conflict of Interest

The authors declare no conflict of interest.

Data Availability Statement

The data that support the findings of this study are available on request from the corresponding author. The data are not publicly available due to privacy or ethical restrictions.

Keywords

interlayer regulations, laminate graphene films, Zn-ion hybrid capacitors, Zn-ion solvation structures

Received: November 28, 2021

Revised: January 11, 2022

Published online:

- [1] L. L. Zhang, X. S. Zhao, *Chem. Soc. Rev.* **2009**, *38*, 2520.
- [2] S. Zhai, H. E. Karahan, C. Wang, Z. Pei, L. Wei, Y. Chen, *Adv. Mater.* **2020**, *32*, 1902387.
- [3] Q. Dou, S. Lei, D.-W. Wang, Q. Zhang, D. Xiao, H. Guo, A. Wang, H. Yang, Y. Li, S. Shi, X. Yan, *Energy Environ. Sci.* **2018**, *11*, 3212.
- [4] P. Simon, Y. Gogotsi, *Nat. Mater.* **2008**, *7*, 845.
- [5] F. Bonaccorso, L. Colombo, G. Yu, M. Stoller, V. Tozzini, A. C. Ferrari, R. S. Ruoff, V. Pellegrini, *Science* **2015**, *347*, 1246501.
- [6] G. Fang, J. Zhou, A. Pan, S. Liang, *ACS Energy Lett.* **2018**, *3*, 2480.
- [7] Z. Ming, J. Fan, C. Bao, Y. Xue, Q. Lin, L. Zhu, *Adv. Funct. Mater.* **2018**, *28*, 1706918.
- [8] C. Li, Z. Sun, T. Yang, L. Yu, N. Wei, Z. Tian, J. Cai, J. Lv, Y. Shao, M. H. Rummeli, J. Sun, Z. Liu, *Adv. Mater.* **2020**, *32*, 2003425.
- [9] J. Li, K. McColl, X. Lu, S. Sathasivam, H. Dong, L. Kang, Z. Li, S. Zhao, A. G. Kafizas, R. Wang, D. J. L. Brett, P. R. Shearing, F. Corà, G. He, C. J. Carmalt, I. P. Parkin, *Adv. Energy Mater.* **2020**, *10*, 2000058.
- [10] C. Xia, J. Guo, Y. Lei, H. Liang, C. Zhao, H. N. Alshareef, *Adv. Mater.* **2018**, *30*, 1705580.
- [11] Y. Shao, Z. Sun, Z. Tian, S. Li, G. Wu, M. Wang, X. Tong, F. Shen, Z. Xia, V. Tung, J. Sun, Y. Shao, *Adv. Funct. Mater.* **2020**, *31*, 2007843.
- [12] M. Song, H. Tan, D. Chao, H. J. Fan, *Adv. Funct. Mater.* **2018**, *28*, 1706918.
- [13] M. Yu, D. Lin, H. Feng, Y. Zeng, Y. Tong, X. Lu, *Angew. Chem., Int. Ed.* **2017**, *56*, 5454.
- [14] Y. Zhang, X. Xia, B. Liu, S. Deng, D. Xie, Q. Liu, Y. Wang, J. Wu, X. Wang, J. Tu, *Adv. Energy Mater.* **2019**, *9*, 1803342.
- [15] F. Mo, G. Liang, Q. Meng, Z. Liu, H. Li, J. Fan, C. Zhi, *Energy Environ. Sci.* **2019**, *12*, 706.
- [16] E. Raymundo-Piñero, K. Kierzek, J. Machnikowski, F. Béguin, *Carbon* **2006**, *44*, 2498.
- [17] C. O. Ania, V. Khomenko, E. Raymundo-Piñero, J. B. Parra, F. Béguin, *Adv. Funct. Mater.* **2007**, *17*, 1828.
- [18] G. Li, K. Mao, M. Liu, M. Yan, J. Zhao, Y. Zeng, L. Yang, Q. Wu, X. Wang, Z. Hu, *Adv. Mater.* **2020**, *32*, 2004632.
- [19] J. Zhang, C. P. Yang, Y. X. Yin, L. J. Wan, Y. G. Guo, *Adv. Mater.* **2016**, *28*, 9539.
- [20] X. Yang, L. Qiu, C. Cheng, Y. Wu, Z. F. Ma, D. Li, *Angew. Chem., Int. Ed.* **2011**, *50*, 7325.
- [21] K. Lee, Y. Yoon, Y. Cho, S. M. Lee, Y. Shin, H. Lee, H. Lee, *ACS Nano* **2016**, *10*, 6799.
- [22] Y. Shao, M. F. El-Kady, C. W. Lin, G. Zhu, K. L. Marsh, J. Y. Hwang, Q. Zhang, Y. Li, H. Wang, R. B. Kaner, *Adv. Mater.* **2016**, *28*, 6719.
- [23] H. Ma, H. Chen, M. Wu, F. Chi, F. Liu, J. Bai, H. Cheng, C. Li, L. Qu, *Angew. Chem., Int. Ed.* **2020**, *59*, 14541.
- [24] H. Li, Y. Tao, X. Zheng, J. Luo, F. Kang, H.-M. Cheng, Q. H. Yang, *Energy Environ. Sci.* **2016**, *9*, 3135.
- [25] J. Chmiola, G. Yushin, Y. Gogotsi, C. Portet, P. Simon, P. L. Taberna, *Science* **2006**, *313*, 1760.
- [26] H. Feng, R. Cheng, X. Zhao, X. Duan, J. Li, *Nat. Commun.* **2013**, *4*, 1539.
- [27] C. Largeot, C. Portet, J. Chmiola, P.-L. Taberna, Y. Gogotsi, P. Simon, *J. Am. Chem. Soc.* **2008**, *9*, 2730.
- [28] Q. Fu, S. Hao, L. Meng, F. Xu, J. Yang, *ACS Nano* **2021**, *15*, 18469.
- [29] M. Hartmann, T. Clark, R. v. Eldik, *J. Am. Chem. Soc.* **1997**, *33*, 7843.
- [30] M. Pavlov, P. E. M. Siegbahn, M. Sandström, *J. Phys. Chem.* **1998**, *102*, 219.
- [31] E. R. Nightingale Jr., *J. Phys. Chem.* **1959**, *63*, 1381.
- [32] Z. Li, S. Gadipelli, H. Li, C. A. Howard, D. J. L. Brett, P. R. Shearing, Z. Guo, I. P. Parkin, F. Li, *Nat. Energy* **2020**, *5*, 160.
- [33] S. Pei, J. Zhao, J. Du, W. Ren, H. M. Cheng, *Carbon* **2010**, *48*, 4466.
- [34] A. C. Forse, C. Merlet, J. M. Griffin, C. P. Grey, *J. Am. Chem. Soc.* **2016**, *138*, 5731.
- [35] A. C. Forse, J. M. Griffin, V. Presser, Y. Gogotsi, C. P. Grey, *J. Phys. Chem. C* **2014**, *118*, 7508.
- [36] J. M. Griffin, A. C. Forse, C. P. Grey, *Solid State Nucl. Magn. Reson.* **2016**, *74*, 16.
- [37] L. Borchardt, M. Oschatz, S. Paasch, S. Kaskel, E. Brunner, *Phys. Chem. Chem. Phys.* **2013**, *15*, 15177.
- [38] H. Zhang, Q. Liu, Y. Fang, C. Teng, X. Liu, P. Fang, Y. Tong, X. Lu, *Adv. Mater.* **2019**, *31*, 1904948.
- [39] W. Zhao, P. Tan, J. Zhang, J. Liu, *Phys. Rev. B* **2010**, *82*, 2955.
- [40] C. Wang, Z. Pei, Q. Meng, C. Zhang, X. Sui, Z. Yuan, S. Wang, Y. Chen, *Angew. Chem., Int. Ed.* **2021**, *60*, 990.
- [41] S. Wu, Y. Chen, T. Jiao, J. Zhou, J. Cheng, B. Liu, S. Yang, K. Zhang, W. Zhang, *Adv. Energy Mater.* **2019**, *9*, 1902915.
- [42] M. F. El-Kady, V. Strong, S. Dubin, R. B. Kaner, *Science* **2012**, *335*, 1326.
- [43] C. Liu, Z. Yu, D. Neff, A. Zhamu, B. Z. Jang, *Nano Lett.* **2010**, *10*, 4863.
- [44] P. Liu, W. Liu, Y. Huang, P. Li, J. Yan, K. Liu, *Energy Storage Mater.* **2020**, *25*, 858.
- [45] J. Li, J. Zhang, L. Yu, J. Gao, X. He, H. Liu, Y. Guo, G. Zhang, *Energy Storage Mater.* **2021**, *42*, 705.
- [46] X. Yang, C. Cheng, Y. Wang, L. Qiu, D. Li, *Science* **2013**, *341*, 534.
- [47] Y. Lu, Z. Li, Z. Bai, H. Mi, C. Ji, H. Pang, C. Yu, J. Qiu, *Nano Energy* **2019**, *66*, 104132.

- [48] Y. Zheng, W. Zhao, D. Jia, Y. Liu, L. Cui, D. Wei, R. Zheng, J. Liu, *Chem. Eng. J.* **2020**, 387, 124161.
- [49] P. Yu, Y. Zeng, Y. Zeng, H. Dong, H. Hu, Y. Liu, M. Zheng, Y. Xiao, X. Lu, Y. Liang, *Electrochim. Acta* **2019**, 327, 134999.
- [50] P. Zhang, Y. Li, G. Wang, F. Wang, S. Yang, F. Zhu, X. Zhuang, O. G. Schmidt, X. Feng, *Adv. Mater.* **2019**, 31, 1806005.
- [51] Z. S. Wu, K. Parvez, X. Feng, K. Mullen, *Nat. Commun.* **2013**, 4, 2487.
- [52] H. Wang, M. Wang, Y. Tang, *Energy Storage Mater.* **2018**, 13, 1.
- [53] Y. Xu, Z. Lin, X. Huang, Y. Liu, Y. Huang, X. Duan, *ACS Nano* **2013**, 7, 4042.
- [54] H. Li, J. Wu, L. Wang, Q. Liao, X. Niu, D. Zhang, K. Wang, *Chem. Eng. J.* **2022**, 428, 131071.
- [55] S. Chen, L. Ma, K. Zhang, M. Kamruzzaman, C. Zhi, J. A. Zapien, *J. Mater. Chem. A* **2019**, 7, 7784.
- [56] L. Dong, X. Ma, Y. Li, L. Zhao, W. Liu, J. Cheng, C. Xu, B. Li, Q. H. Yang, F. Kang, *Energy Storage Mater.* **2018**, 13, 96.
- [57] C. Choi, J. A. Lee, A. Y. Choi, Y. T. Kim, X. Lepro, M. D. Lima, R. H. Baughman, S. J. Kim, *Adv. Mater.* **2014**, 26, 2059.
- [58] X. Chen, L. Qiu, J. Ren, G. Guan, H. Lin, Z. Zhang, P. Chen, Y. Wang, H. Peng, *Adv. Mater.* **2013**, 25, 6436.
- [59] Y. Meng, Y. Zhao, C. Hu, H. Cheng, Y. Hu, Z. Zhang, G. Shi, L. Qu, *Adv. Mater.* **2013**, 25, 2326.
- [60] J. A. Lee, M. K. Shin, S. H. Kim, H. U. Cho, G. M. Spinks, G. G. Wallace, M. D. Lima, X. Lepro, M. E. Kozlov, R. H. Baughman, S. J. Kim, *Nat. Commun.* **2013**, 4, 1970.
- [61] Z. Li, S. Gadipelli, Y. Yang, G. He, J. Guo, J. Li, Y. Lu, C. A. Howard, D. J. L. Brett, I. P. Parkin, F. Li, Z. Guo, *Energy Storage Mater.* **2019**, 17, 12.
- [62] L. F. Chen, Z. H. Huang, H. W. Liang, W. T. Yao, Z. Y. Yu, S. H. Yu, *Energy Environ. Sci.* **2013**, 6, 3331.
- [63] M. D. Stoller, S. Park, Y. Zhu, J. An, R. S. Ruoff, *Nano Lett.* **2008**, 8, 3498.
- [64] X. Wang, C. Lu, H. Peng, X. Zhang, Z. Wang, G. Wang, *J. Power Sources* **2016**, 324, 188.
- [65] S. Murali, N. Quarles, L. L. Zhang, J. R. Potts, Z. Tan, Y. Lu, Y. Zhu, R. S. Ruoff, *Nano Energy* **2013**, 2, 764.
- [66] Y. Li, W. Yang, W. Yang, Z. Wang, J. Rong, G. Wang, C. Xu, F. Kang, L. Dong, *Nano-Micro Lett.* **2021**, 13, 95.
- [67] Y. Xu, Z. Lin, X. Zhong, X. Huang, N. O. Weiss, Y. Huang, X. Duan, *Nat. Commun.* **2014**, 5, 4554.
- [68] A. Izadi-Najafabadi, S. Yasuda, K. Kobashi, T. Yamada, D. N. Futaba, H. Hatori, M. Yumura, S. Iijima, K. Hata, *Adv. Mater.* **2010**, 22, E235.
- [69] Z. Li, D. Chen, Y. An, C. Chen, L. Wu, Z. Chen, Y. Sun, X. Zhang, *Energy Storage Mater.* **2020**, 28, 307.
- [70] T. Kim, G. Jung, S. Yoo, K. S. Suh, R. S. Ruoff, *ACS Nano* **2013**, 7, 6899.
- [71] Y. Tao, X. Xie, W. Lv, D. M. Tang, D. Kong, Z. Huang, H. Nishihara, T. Ishii, B. Li, D. Golberg, F. Kang, T. Kyotani, Q. H. Yang, *Sci. Rep.* **2013**, 3, 2975.
- [72] J. Zhong, W. Sun, Q. Wei, X. Qian, H. M. Cheng, W. Ren, *Nat. Commun.* **2018**, 9, 3484.
- [73] D. Yu, K. Goh, H. Wang, L. Wei, W. Jiang, Q. Zhang, L. Dai, Y. Chen, *Nat. Nanotechnol.* **2014**, 9, 555.
- [74] F. Meng, Y. Ding, *Adv. Mater.* **2011**, 23, 4098.
- [75] Q. Zhang, Y. Ma, Y. Lu, L. Li, F. Wan, K. Zhang, J. Chen, *Nat. Commun.* **2020**, 11, 4463.
- [76] L. Cao, D. Li, E. Hu, J. Xu, T. Deng, L. Ma, Y. Wang, X. Q. Yang, C. Wang, *J. Am. Chem. Soc.* **2020**, 142, 21404.
- [77] G. Sun, H. Yang, G. Zhang, J. Gao, X. Jin, Y. Zhao, L. Jiang, L. Qu, *Energy Environ. Sci.* **2018**, 11, 3367.
- [78] M. Chen, J. Chen, W. Zhou, J. Xu, C. P. Wong, *J. Mater. Chem. A* **2019**, 7, 26524.
- [79] P. Huang, C. Lethien, S. Pinaud, K. Brousse, R. Laloo, V. Turq, M. Respaud, A. Demortière, B. Daffos, P. L. Taberna, B. Chaudret, Y. Gogotsi, P. Simon, *Science* **2016**, 351, 691.
- [80] A. Mahmood, Z. Yuan, X. Sui, M. A. Riaz, Z. Yu, C. Liu, J. Chen, C. Wang, S. Zhao, N. Mahmood, Z. Pei, L. Wei, Y. Chen, *Energy Storage Mater.* **2021**, 41, 395.
- [81] J. P. Perdew, K. Burke, M. Ernzerhof, *Phys. Rev. Lett.* **1996**, 78, 1396.
- [82] S. Grimme, S. Ehrlich, L. Goerigk, *J. Comput. Chem.* **2011**, 32, 1456.